INTERFACE

Research

Check for updates

Authors for correspondence:
Amanda K. Stowers
e-mail: astowers@stanford.edu
David Lentink
e-mail: dlentink@stanford.edu

THE ROYAL SOCIETY
PUBLISHING

How pigeons couple three-dimensional elbow and wrist motion to morph their wings

Amanda K. Stowers, Laura Y. Matloff and David Lentink

Department of Mechanical Engineering, Stanford University, 416 Escondido Mall, Stanford, CA 94305, USA

AKS, 0000-0003-4673-9524; LYM, 0000-0002-2033-2243; DL, 0000-0003-4717-6815

Birds change the shape and area of their wings to an exceptional degree, surpassing insects, bats and aircraft in their ability to morph their wings for a variety of tasks. This morphing is governed by a musculoskeletal system, which couples elbow and wrist motion. Since the discovery of this effect in 1839, the planar 'drawing parallels' mechanism has been used to explain the coupling. Remarkably, this mechanism has never been corroborated from quantitative motion data. Therefore, we measured how the wing skeleton of a pigeon (*Columba livia*) moves during morphing. Despite earlier planar assumptions, we found that the skeletal motion paths are highly three-dimensional and do not lie in the anatomical plane, ruling out the 'drawing parallels' mechanism. Furthermore, micro-computed tomography scans in seven consecutive poses show how the two wrist bones contribute to morphing, particularly the sliding ulnare. From these data, we infer the joint types for all six bones that form the wing morphing mechanism and corroborate the most parsimonious mechanism based on least-squares error minimization. Remarkably, the algorithm shows that all optimal four-bar mechanisms either lock, are unable to track the highly three-dimensional bone motion paths, or require the radius and ulna to cross for accuracy, which is anatomically unrealistic. In contrast, the algorithm finds that a six-bar mechanism recreates the measured motion accurately with a parallel radius and ulna and a sliding ulnare. This revises our mechanistic understanding of how birds morph their wings, and offers quantitative inspiration for engineering morphing wings.

1. Introduction

The ability of birds to change and streamline the shape of their wings from fully extended to swept back distinguishes them from insects, bats, pterosaurs and aircraft (figure 1). Wing morphing broadens the performance envelope of birds, enabling them to fly faster, longer, and manoeuvre more effectively [14–18]. Underlying the ability to morph is a musculoskeletal mechanism first documented in an anatomical study of cadavers by Bergmann in 1839 [1]. This mechanism is thought to automatically flex and extend the wing like a four-bar 'drawing parallels' [1–4] (figure 1b). This four-bar mechanism follows from the specialized skeletal arrangement of a bird wing; the upper arm bone, the humerus, connects to two lower arm bones, the radius and ulna, which connect via the wrist to the carpometacarpus (figure 1d). In contrast to other vertebrates (figure 1c), the parallel arrangement of the radius and ulna coordinates elbow and wrist joint motions in birds. In non-flying vertebrates, the radius and ulna are either rotated relative to the elbow along the longitudinal axis of the humerus (e.g. approx. 90° in humans), or fused together (e.g. ungulates). Even among flying vertebrates, birds and their ancestors have a unique bone arrangement. Bats fly competently with a rudimentary ulna that does not connect to the wrist [5]. Similarly, pterosaurs had a straight radio-ulna, lacking the curvature and separation needed for a functional four-bar mechanism [19]. Consequentially, birds can morph their wings more than
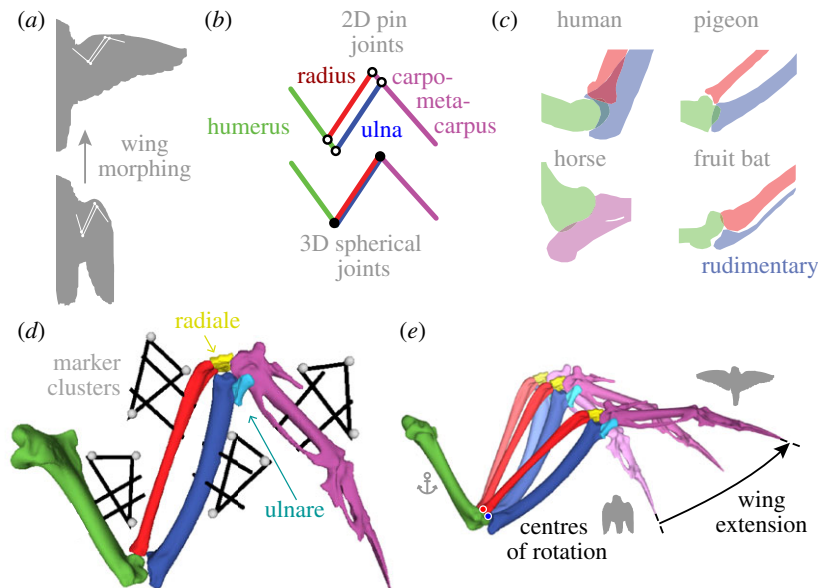
Figure 1. Bird wing flexion and extension (morphing) is coordinated by a unique musculoskeletal structure that functions analogously to a mechanical linkage with a single degree of freedom. (*a*) The skeleton morphs the wing, which includes shape, span, sweep and area. (*b*) The current paradigm for explaining avian wing morphing is the qualitative two-dimensional 'drawing parallels' mechanism in which the wing moves in a plane, and the elbow and wrist are coupled by a single degree of freedom [1–6]. More recent computational and biological models assume a fused radius and ulna (drawn side-by-side in schematic) with three-dimensional spherical joints at the elbow and wrist [7–11], which simplifies elbow and wrist function and ignores three-dimensional coupling [12,13]. (*c*) Contrasting the ventral view of the elbow joint in birds versus other vertebrates provides a clue about how the coupling works. Relative to a human, the bird radius and ulna articulation is rotated by 90° with respect to the longitudinal axis of the humerus. Therefore, bending the elbow pushes the radius along the ulna in birds, which abducts the wrist. In contrast, other vertebrates' radius and ulna articulation prevents this coupling. For instance, horses and other ungulates tend to have fused forelimb bones. Bats, on the other hand, have a similar elbow configuration as birds, but have a rudimentary ulna, prohibiting elbow–wrist coupling. (*d,e*) In this study, we measured the motion of pigeon bones using two techniques. (*d*) First, we implanted clusters of three markers into each of the large (humerus, radius, ulna, carpometacarpus) bones and measured their motion using motion capture. (*e*) Second, we made micro-computed tomography scans of the forelimb in seven poses (three shown) to determine the motion of all the bones including the radiale and ulnare wrist bones. The anchor indicates the stationary bone to show the relative motion of other bones.

bats and pterosaurs while continuously maintaining an aero-dynamic profile [20]. This suggests that the precise arrangement of the ulna and radius is important to understand the evolution and function of avian flight. The orientation of the radius and ulna is a striking feature present even in the fossil remains of their dinosaur ancestors such as *Archaeopteryx* [21].

In vivo and anatomical evidence demonstrates that the coupling of elbow and wrist motion is critical for birds to fly well. The 'drawing parallels' function of the radius and ulna has been tested with *in vivo* surgical manipulations in pigeons by Fisher [2], confirming elbow–wrist coupling. Furthermore, injured birds lacking the ability to move their radius and ulna relative to each other have difficulty flying. For instance, a Mississippi kite (*Ictinia mississippiensis*) whose radius and ulna fused together after a fracture could no longer extend its wings or fly [22]. After surgical separation, the bird regained its wing motion and flight abilities, indicating that relative radio-ulnar motion is important. In a similar situation, a barn owl (*Tyto alba*) whose radius was severely injured and amputated had less wrist stability and was unable to fully extend its hand wing [23]. Finally, Vazquez [12] showed in an anatomical study of a pigeon wing how the specific attachment of muscles, tendons and other connective tissues helps create the coupled motion of the elbow and wrist joints.

Existing kinematic models of bird wings consider the wing as either a planar four-bar mechanism with unspecified parameters [1,4,5,12] or a specified open kinematic chain starting at the shoulder with the radius and ulna fused as a single bone [7–9,24]. These kinematic-chain studies offer insight into joint angles, but do not consider more anatomically realistic mechanism types. Additionally, all existing kinematic models ignore the role of the two wrist bones [7–9], despite anatomical studies suggesting that the wrist bones move and help coordinate hand motion [13]. More sophisticated quantitative models of musculoskeletal arm and wrist motion exist only for humans [25–28]. These models have been corroborated from the recorded kinematics of bones in human cadavers by implanting markers and animating the arm and hand through their degrees of freedom. Despite their homology, human and bird forelimbs move completely differently due to the morphological specialization visible in the ventral view (figure 1*c*), which makes human models irrelevant for understanding wing morphing. However, the detailed motion capture and model corroboration techniques can be miniaturized and adapted for a bird cadaver.

To test the hypothesis that the avian forelimb functions as a four-bar mechanism in which wrist bone function can be ignored [1–5], we measured wing skeletal kinematics in pigeon cadavers. We measured humerus, radius, ulna and carpometacarpus motion by motion tracking implanted marker clusters, and related marker to bone motion and bone shape using micro-computed tomography (μCT) scans. We made additional μCT scans of the wing in seven different poses to determine the relative motion of the four bones with respect to the much smaller wrist bones, the radiale and ulnare, since they were too small to be tracked using motion capture. Using established joint optimization

techniques, we found that a six-bar mechanism with a fully functional wrist represents the most parsimonious kinematic model of the avian forelimb. Subsequent mathematical optimization demonstrated how four-bar models only represent the data well when the ulna and radius cross, which is anatomically unrealistic. This not only revises our textbook understanding of avian functional morphology [5,6,19], but may critically inform fossil interpretation [29] and developmental studies [22,23]. Finally, the six-bar model offers the first quantitative information for avian-inspired morphing wing design [30–33].

2. Material and methods

To corroborate the mechanism underpinning bird wing morphing, we measured the linear and rotational motion of wing bones by animating the wings of three racing pigeon cadavers (*Columba livia*; $N = 3$; electronic supplementary material, table S1). To objectively determine the most parsimonious forelimb mechanism, we used a mathematical performance evaluation based on error minimization, which requires high resolution of all six degrees of freedom, including rotation about the long axis of individual bones. This requirement ruled out *in vivo* methods based on high-speed fluoroscopy [10,34,35], because the approximately 1 MP resolution of the image intensifiers is too low. At present we find that these limitations can only be overcome by cadaver studies, similar to those performed in humans [26–28]. To achieve high fidelity measurements, we used 12 MP resolution motion capture in concert with μCT scans that offer the small error required for automated mathematical analysis. We used the motion capture system to measure the relative positions of the four large wing bones during a large number of continuous wing pose changes. We complemented the bone motion recordings with μCT scans to determine the bone shapes and the relative location of the bone markers. Additionally, we scanned the wings in seven poses to determine the motion of the much smaller wrist bones, which could not be fitted with marker clusters.

2.1. High-resolution motion capture and micro-computed tomography scans of the wing skeleton

To track skeletal motion for each of the birds, we manually morphed the right wing following the path of least resistance while tracing out measured pigeon wing shapes (figure 1*d,e*). The pigeons were fully intact except that covert feathers were removed to allow for bone implantation of the motion tracking markers. Unique marker clusters (electronic supplementary material, table S2) were adhered to two carbon fibre posts (1 mm) implanted ventrally in the keel of the sternum, humerus, radius, ulna and carpometacarpus. Each marker cluster consisted of three 2.4 mm diameter retroreflective markers (B&L Engineering) that were glued (BSI Super Gold) to scalene triangles made from hollow carbon fibre rods (0.7 mm). We used Monte Carlo simulations [36] to choose the distances between markers in each cluster such that they were optimal for automatic identification. To do this, we tested randomized lengths for each cluster edge and tested how well the markers were identified for each set. We then chose a case where identification was possible more than 98% of the time. With these uniquely identifiable marker clusters in place, we measured bone motion by mounting the pigeon cadaver to a custom support frame and moving the wing through a series of three motion types actuated by hand from the carpometacarpus. The three motion types were as follows: (i) wing flexion and extension traced through the three wing outlines reported for a pigeon gliding at different speeds [14,37], (ii) wrist circumduction with the elbow held by hand at approximately mid-extension, and (iii) range of wrist rotation with the elbow held by hand at approximately mid-extension. Whereas only the flexion and extension cycle was used to determine the coupling between the elbow and wrist during morphing, all three motion types were used to determine the motion space of the wing joints. For each of the three motion types, we conducted five trials, moving the wing by hand at 0.5 Hz per cycle for 25 s. We used a metronome to time wing motion and ensure equivalent data between all pigeons. Six cameras were used for tracking markers and a seventh for visual marker verification in video mode (cameras: Qualisys, Oqus 7+, 12 MP at 300 Hz, video mode at 30 Hz), with an accuracy of approximately 0.1 mm (standard deviation of wand length, tracking done by Qualisys Track Manager; QTM 2.11). After motion tracking, we separated the right wing from the body and measured the three-dimensional geometry of the skeleton and relative positions of the implanted markers with μCT scans (GE eXplore RS150, 47 μm voxels). Finally, we separated the left wing to measure the relative positions of the four large wing bones and the radiale and ulnare wrist bones in concert. To determine the relative motion of the bones from pose to pose, we μCT scanned seven wing poses (Siemens Inveon mm-PET/CT 43 μm voxels), segmented the bones and then aligned them to each position manually in Meshlab (v. 1.3.3).

2.2. Calculation of bone positions and joint locations

Using the motion capture data, we exported bone trajectories into Matlab (The Mathworks, R2015b) and filtered the position data with a fourth order low-pass Butterworth filter at 8 Hz. We defined the flexion–extension cycles using the periodic motion of the most distal point on the carpometacarpus. Each flexion–extension cycle lasted approximately two seconds, so we resampled the data to 500 points per cycle for consistency. We automatically generated the mechanisms using the cycles for which all markers were successfully tracked for at least 80% of the time ($n = 83$), and subsequently validated these mechanisms using cycles for which all markers successfully tracked 100% of the time ($n = 37$ total; $n = 14$ for pigeon 1, $n = 9$ for pigeon 2, $n = 14$ for pigeon 3). By tracking three markers on each of the humerus, radius, ulna and carpometacarpus, we determined all rotations as well as translations of these bones relative to each other. For the radiale and ulnare, orientation was determined using the seven μCT-scanned poses. To achieve consistency in our numerical analysis and to compare fairly between pigeons, we defined theoretical markers located at the centre of mass and 30 mm along the principal axes of each measured bone and used those for calculations (calculated assuming uniform density in Meshlab v. 1.3.3), as shown in electronic supplementary material, figure S1.

2.3. Mechanism corroboration via error minimization

We corroborated mechanisms based on the motion capture and μCT data using a custom programmed (The Mathworks, Matlab 2015b) least-squares method to determine the centres and axes of rotation for each model bone [38]. We constructed the joints between the more distal 'moving' bone, m, and the more proximal 'grounded' bone, g, as follows. For each frame, k, computational markers are located on the bone at $v_1 = [0, 0, 0]^T$, $v_2 = [0, 30, 0]^T$, $v_3 = [0, 0, 30]^T$, $v_4 = [30, 0, 0]^T$, shown in electronic supplementary material, figure S1. These positions are identifiable across pigeons. They also make the calculation of the centres of rotation less sensitive to errors in marker measurement, because at least three of these points are not expected to lie close to a line intersecting with the centre of rotation. The position vector $p_{i,o,k}$ corresponds to the centre of mass (o; origin), and the unit vectors $\hat{p}_{i,x,k}$, $\hat{p}_{i,y,k}$, $\hat{p}_{i,z,k}$ correspond to the unit

principal axes (x, y, z). To calculate the positions of the moving computational bone markers in the ground bone reference frame we first compute the rotation matrix

$$R_{i,k} = \begin{bmatrix} \hat{p}_{i,x,k} & \hat{p}_{i,y,k} & \hat{p}_{i,z,k} \end{bmatrix} \quad (2.1)$$

to construct the transformation matrix

$$T_{i,k} = \begin{bmatrix} R_{i,k} & p_{i,0,k} \\ 0 & 1 \end{bmatrix} \quad (2.2)$$

which enables us to calculate the computational marker positions of the moving bone in the fixed bone reference frame:

$$\begin{bmatrix} v_k^p \\ 1 \end{bmatrix} = T_{g,k}^{-1} T_{m,k} \begin{bmatrix} v_p \\ 1 \end{bmatrix}. \quad (2.3)$$

Based on the relative positions of the moving bone over the course of the flexion–extension cycle we calculated the best-fit average position for the joint between the bones. For mechanical simplicity, we restricted the joint types between pairs of adjacent bones to spherical joints (three rotational degrees of freedom), pin joints (one rotational degree of freedom), and slider joints (one translational degree of freedom) [39]. We calculated the best fit axes between each pair of bones using a least-squares method [38]. This method minimizes the effects of errors from marker motion and camera calibration on the calculated positions of the predicted joints [40]. The locations of the centres of rotation of spherical joints, the axis of rotation of pin joints and the axis of translation of slider joints were thus calculated as follows:

$$v_{\text{position}} = \left(2 \sum_{p=1}^{3} \left[\left\{ \frac{1}{N} \sum_{k=1}^{N} v_k^p (v_k^p)^T \right\} - \left(\frac{1}{N} \sum_{k=1}^{N} v_k^p \right) \left(\frac{1}{N} \sum_{k=1}^{N} v_k^p \right)^T \right] \right)^{-1}$$
$$\sum_{p=1}^{3} \left[\frac{1}{N} \sum_{k=1}^{N} (v_k^p)^2 v_k^p - \left(\frac{1}{N} \sum_{k=1}^{N} v_k^p \right) \frac{1}{N} \sum_{k=1}^{N} (v_k^p)^2 \right]$$
$$(2.4)$$

in which N is the total number of observed marker time steps across all flexion–extension cycles that met the threshold marker observation selection criteria, which we repeated for each of the three pigeons. For pin and slider joints we also needed to calculate the average orientation of the joint, which is the minimum eigenvector of the following matrix:

$$2 \sum_{p=1}^{3} \left[\left\{ \frac{1}{N} \sum_{k=1}^{N} v_k^p (v_k^p)^T \right\} - \left(\frac{1}{N} \sum_{k=1}^{N} v_k^p \right) \left(\frac{1}{N} \sum_{k=1}^{N} v_k^p \right)^T \right]. \quad (2.5)$$

To create closed-loop mechanisms that model the coupled motion between the elbow and wrist, we used the wing in its extended position as a reference point for creating the mechanism and calculating error based on the motion capture data. For the µCT data, the extended reference point occurred at about three-quarters of the fully extended motion capture position. This explains why our mechanisms generally fit the data better in the fully extended position. We corroborated four-bar mechanisms from the skeletal motion capture data as well as four-, five- and six-bar mechanisms from the seven µCT scans per pigeon. We imported each mechanism with the calculated axes into 3D OpenSim models (v. 3.3) [41], where we calculated and visualized its motion. Subsequently, we used the OpenSim Inverse Kinematics tool to test how well each mechanism approximated the measured data. We evaluated tracking performance based on the difference between the measured and modelled kinematics of each cycle as

$$\text{error} = \sqrt{\frac{1}{k_{\max}} \sum_{k=1}^{k_{\max}} \frac{1}{i_{\max}} \sum_{i=1}^{i_{\max}} ||v_{i,t,\text{measured}} - v_{i,t,\text{modeled}}||^2} \quad (2.6)$$

with time step, k, maximum number of steps per cycle, $k_{\max}$, individual marker number, i, and maximum number of markers,
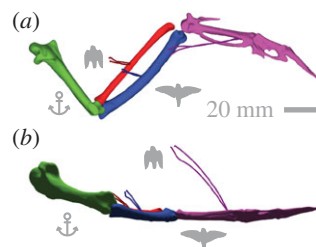
Figure 2. Wing skeletal motion does not coincide with the anatomical plane and is non-planar during flexion and extension. (*a*) Looking from the ventral view with the humerus fixed (anchored), we see the motion paths of the bone centres of mass (coloured lines) move mediolaterally as expected. (*b*) Looking anteriorly (from the tail), we see how the carpometacarpus moves significantly out of the anatomical plane defined by the humerus and radius/ulna. Electronic supplementary material, video S1, shows an animation of this motion from both viewpoints. Coloured lines represent the motion paths of the bone centres of mass in both panels.
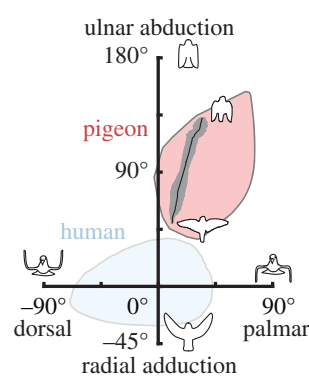
Figure 3. During wing flexion and extension, the hand wing primarily moves in abduction and adduction with a small amount of palmar and dorsal flexion following a specific limit cycle path (black line and grey area, average and s.d. for three birds). While flexion and extension adjustments during gliding may be large, they make up only a fraction of the overall morphing capability of a pigeon wing. In addition, the entire bird wrist motion space is disjoint with the range of human wrist motion (from [42]), showing how birds cannot fully straighten their wrist to achieve a radioulnar deviation of zero. Earlier studies have shown this permanent abduction of the wrist enables wing folding [29]. (Wrist angle definitions are further shown in electronic supplementary material figure S2.)

$i_{\max}$. Finally, we calculated the number of degrees of freedom of each mechanism using the mobility equation for three-dimensional mechanisms [39]:

$$v_{\text{DOF}} = 6(m_{\text{bars}} - 1) - 5m_{\text{pin}} - 5m_{\text{slider}} - 3m_{\text{spherical}} \quad (2.7)$$

in which v represents the number of degrees of freedom and m represents the number of bars or joints in a particular mechanism. Mechanisms with more degrees of freedom require more actuators, or muscles, and are therefore more difficult to control, but can move through more types of motion. In this paper, we assess families of mechanisms including either all six bones or only the four large wing bones to determine how well they represent the data. This produces a total of 83 mechanisms with degrees of freedom (DOF) ranging from 0 DOF, a locked wing that cannot move, to 8 DOF, which includes the degrees of freedom of the wrist joint.

3. Results and discussion

Based on the motion capture study of the pigeon wing skeleton (figure 1), we find that wing morphing is coordinated
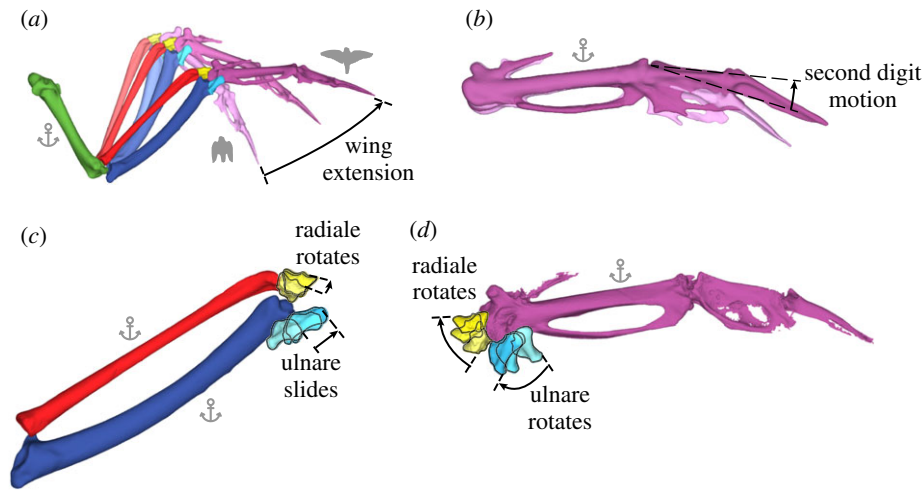
Figure 4. During wing flexion and extension, the second digit can move independently while the wrist bones rotate and slide in concert with the connecting bones. We show the bones here in three (out of seven) positions obtained with μCT scans (other pigeons shown in electronic supplementary material, figure S3). (*a*) As the wing extends, the elbow and wrist move in a coordinated fashion. (*b*) The second digit can move independently up to 30°, enabling refinement of wingtip motion. (*c*) Relative to the lower radius and ulna, the ulnare primarily slides along the ulna while the radiale remains relatively stationary. (*d*) Both the radiale and ulnare primarily rotate about the head of the carpometacarpus.

by three-dimensional bone motion beyond the anatomical plane, defined as the plane spanning the humerus and the radius/ulna. In the fully extended wing position, the humerus, radius, ulna and carpometacarpus lie primarily in this plane. At the maximally flexed position, the plane spanned by the radius/ulna and the carpometacarpus deviates from the anatomical plane by about 45°. However, as the wing flexes, the large wing bones deviate from the best fit wing motion plane (figure 2) by an average of 5.0 ± 0.7 mm for all three pigeons. This deviation means that a planar mechanism could have a minimum error of 5 ± 0.7 mm, showing that even the best possible two-dimensional mechanism would perform worse than three-dimensional mechanisms. Therefore, the planar four-bar mechanism paradigm, inferred from anatomical studies since 1839 [1–3,5,6], does not represent measured skeletal motion, which is highly three-dimensional. To better quantify the full range of motion of the wing, we measured the range of possible motion of the carpometacarpus relative to the radius/ulna, both in and out of the anatomical plane (figure 3; angles defined in electronic supplementary material, figure S2). The wing flexion and extension adjustments during gliding represent a well-defined narrow path within the full range of potential wrist motion (shaded area). The remainder of the motion space is available for wing control adjustments, wing flapping, or folding the wings against the body. For comparison, we also plotted the range of motion for a human wrist [42] in figure 3. This illustrates how bird wrists have permanent ulnar abduction with the hand angled towards the ulnar side of the forearm, [29] compared to the human wrist [42]. This provides wrist stabilization [13] and locks the wing in place during lift generation so it can bear the extreme load, which is proportional to body weight. Together these adaptations explain why human and bird wrist motion spaces do not overlap, despite the fact that the full wrist motion space of a bird has about the same area as that of a human. The bird flexion–extension limit cycle only occupies a narrow region of wrist motion space; the additional area facilitates palmar folding during

flapping flight and fully folding the wing to the body. In concert, these quantitative observations of three-dimensional bird skeletal motion explain why a new data-driven mechanism is needed to underpin the three-dimensional skeletal kinematics of bird wing morphing.

A six-bar model of the wing skeleton including the two wrist and four main wing bones represents the measured three-dimensional skeletal kinematics and morphology well. We created this mechanism by combining anatomical observations from μCT scans with simplified joint models defined and evaluated using least-squares error minimization (Material and methods). This process is similar to the one developed for analysing and modelling the measured skeletal motion in biomedical studies of the human arm [26]. We initialized our model by integrating the measured relative motion of the two wrist and four main wing bones in the seven μCT scans that span the wing flexion–extension cycle (figure 4), combined with earlier qualitative studies [9,12]. Based on this evaluation, we hypothesize the following possible joint types between the wing bones: two spherical joints connect the distal end of the humerus with the proximal end of the radius and ulna, a pin joint connects the distal radius with the radiale, a slider joint connects the distal ulna with the ulnare, and two spherical joints connect the radiale and ulnare with the proximal end of the carpometacarpus. These joints together comprise 8 DOF for the wing. The associated lengths of all six bars as well as the locations, orientations and motions of the joints, figure 5*a*, were calculated using a modified least-squares algorithm (Material and methods) [43] for each of the three pigeons. To account for differences in bone length between the three individuals, we created topologically equivalent models that were scaled to fit each pigeon. For each mechanism, we quantified the mechanism prediction error over the whole flexion–extension cycle (figure 5*b*), which remains fairly constant and is of similar magnitude across all flexion and extension cycles of each wing. This corroborated six-bar model predicts anatomically reasonable locations for the joint locations and the lengths of the connecting bars, as well as joint motion paths of the four
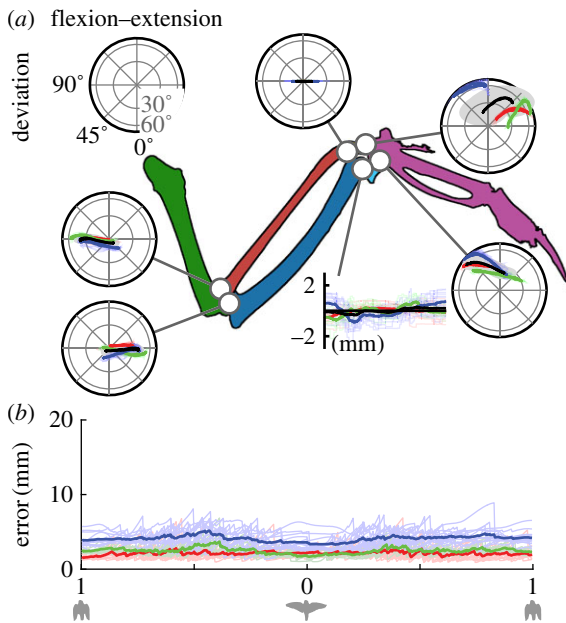
Figure 5. By applying error minimization to the motion capture and μCT scan data, we corroborated a six-bar mechanism that accurately represents the three-dimensional coupled motion of wing morphing. The mechanism uses four spherical joints to connect the humerus and carpometacarpus and a pin (radiale) and slider joint (ulnare) for the wrist bone joints. In this mechanism, the radiale and ulnare are single degree of freedom extensions of the radius and ulna respectively. (a) Using the six-bar model, we calculated all joints required to replicate the measured CT scan data using a least-squares error minimization algorithm. The circular plots show the motion space for a spherical joint, with the centre representing the centre of rotation. Straight lines through the centre represent the best fit pin joint, while deviation from this represents spherical joints. Long axis rotation is not shown (involved in wing pronation and supination, which we did not study). Spherical joints at the elbow move more similarly to pin joints compared to those connecting the carpometacarpus to the wrist. The radiale and ulnare each move less than the large bones, with less than 4 mm total ulnare excursion during a typical cycle. (b) The root mean square error of the simulated markers (see Material and methods, equation (2.6)) is shown over the flexion and extension cycle for each of the three pigeons and is nearly constant (error calculation based on motion capture data of the four large bones; jumps are due to meeting convergence criteria in the error minimization scheme). Thick coloured lines indicate average results for each pigeon (red, pigeon 1; green, pigeon 2; blue, pigeon 3), individual traces are indicated with semitransparent thinner lines. The thick black lines show the average over all three pigeons and the grey areas represent standard deviation. The schematic is based on pigeon 1.

spherical, one pin and one slider joints (figure 5). The best-fit joint paths over each sphere show that the elbow joints behave relatively closely to pin joints, with predominant elbow flexion–extension. In contrast, the joint between the wrist bones and the carpometacarpus requires the ranges of motion provided by a spherical joint, due to significant wrist abduction/adduction and palmar/dorsal motion. Additionally, the relative radius–radiale, and ulna–ulnare motion is small, which explains why a pin and slider joint are sufficient to approximate their degrees of freedom (figure 4). The six bars and the six measured joint motion paths combined define the flexion and extension cycle of the pigeon wing, during gliding, with a quasi-single degree of freedom (figure 5). Based on this six-bar model, we adjusted the number of bars and joint types to establish the
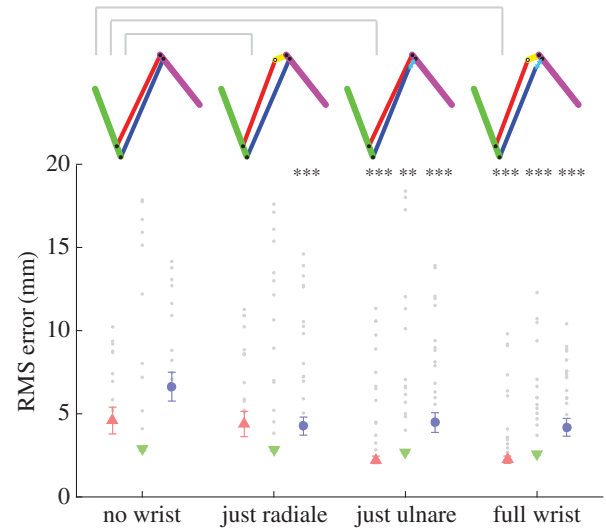
Figure 6. Using a least-squares error minimization algorithm, we find that including the wrist bones in the mechanism is essential to replicate the measured skeletal motion accurately. We calculated the RMS errors for all permutations in which we change spherical joints into pin joints, while keeping sufficient degrees of freedom to not lock the mechanism (shown as grey circles). From this we found that the four spherical joints in our model (figure 5) are essential for minimal RMS error (coloured symbols) regardless of how we simplified the wrist. To determine if modelling wrist motion is essential, we fused both wrist joints (no wrist), the ulnare (just radiale), and the ulnare (just radiale) at their fully extended location and compared it with the full wrist model (figure 5). Using a t-test, we find that for all three pigeons a sliding ulnare significantly improves the ability of a mechanism to replicate measured skeletal motion, and that the combination of the radiale and ulnare reduces RMS error ($p < 0.001$; see details in table 1). Sketches denote line diagrams of each mechanism manipulation, which are drawn to scale based on pigeon 1. The three columns for each mechanism indicate the three different pigeons tested (red, green and blue are used for their corresponding minimal RMS error mechanisms). Definitions for mechanisms shown on top: solid line, bar; solid circle, 3 DOF spherical joint; open circle, 1 DOF pin joint; double arrow, 1 DOF slider joint. See electronic supplementary material, video S2, for a comparison of the fused four-bar 'no wrist' and six-bar 'full wrist' mechanism.

most parsimonious model that can accurately represent the measured skeletal motion.

Systematic tests show that a simplified six-bar skeletal model of the pigeon wing, with a reduced number of bars and degrees of freedom, fits the data worse than the original six-bar model. We tested simpler models not only to assess parsimony, but also to verify earlier models that have suggested that the wrist bones can be ignored [1–3,5,7, 9–11] and that the bones connect like pin joints at the elbow [7,9]. We therefore simplified the corroborated six-bar model to see how earlier mechanism choices affect tracking performance and morphological realism. We found that converting one or more spherical joints into pin joints increased the RMS error of all simplified mechanism permutations tested (grey dots in figure 6). The effect of constraining motion to a pin joint is not equal for all joints. Generally speaking, constraining the elbow caused less increase in error than constraining the wrist; however, the best performance occurs with spherical joints, because they track the three-dimensional motion out-of-anatomical-plane better (figures 2, 4 and 5). To determine if simplifying the wrist affects tracking performance, we first removed the radiale
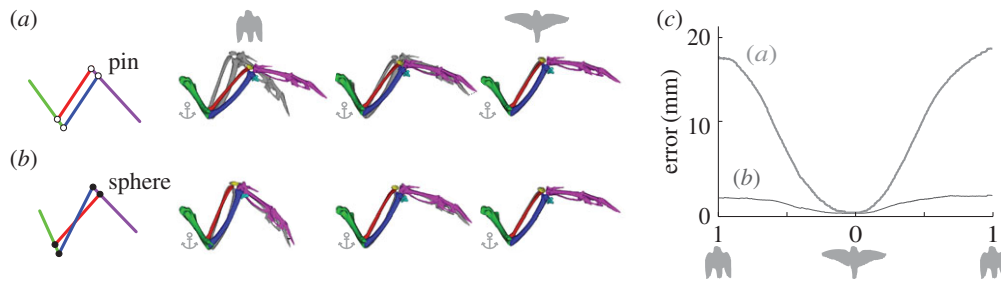
Figure 7. The 'drawing parallels' paradigm cannot explain bird skeletal motion during wing morphing, because the four-bar mechanisms that fit the three-dimensional motion data require the radius and ulna bars to cross, which is anatomically unrealistic. (a) The pin joints of a 'drawing parallels' mechanism lock along the highly three-dimensional skeletal motion paths of wing flexion and extension. We anchored the humerus to show relative bone motion. (b) A four-bar mechanism with spherical joints replicates the bone motion accurately. However, the error minimization requires the mechanism to cross, which does not match the scanned skeletal motion data. (c) The RMS error of the locked (a) and crossed (b) four-bar mechanisms over the flexion–extension cycle. The mechanisms approximate motion best at the fully extended position because the mechanism creation algorithm uses that as the starting position. In both (a) and (b), coloured bones indicate four-bar mechanism motion based on error minimization, grey bones indicate measured motion.

Table 1. Including the wrist bones in the corroborated skeletal mechanism is essential for tracking the measured bone motion accurately. Including wrist bones in the mechanism decreases the kinematics tracking error for each pigeon statistically significantly. Additionally, paired sample testing rejects the hypothesis that the wrist bones have no effect with $p < 0.001$ (t-test, the 95% CI of decrease in error by incorporating wrist bones is $1.5 - 2.3$ mm). Including the ulnare significantly improves the wing mechanism performance for each pigeon, while including the radiale only improves wing mechanism performance for one pigeon. Therefore, we conclude that the motion of the ulnare is important for understanding bird wing flexion–extension, while the role of the radiale is less important. (Parameter n is the number of wing flexion–extension cycles with 100% tracking, which we used for mechanism validation.)

	n	locked wrist RMS error (mm)	just radiale RMS error (mm)	just ulnare RMS error (mm)	full wrist RMS error (mm)
pigeon 1	14	4.6 ± 0.8	4.4 ± 0.8	2.2 ± 0.2***	2.2 ± 0.2***
pigeon 2	9	2.9 ± 0.1	2.8 ± 0.1	2.7 ± 0.1**	2.6 ± 0.1***
pigeon 3	14	6.6 ± 0.9	4.3 ± 0.5***	4.5 ± 0.6***	4.2 ± 0.5***

**$p \leq 0.01$, ***$p \leq 0.001$.
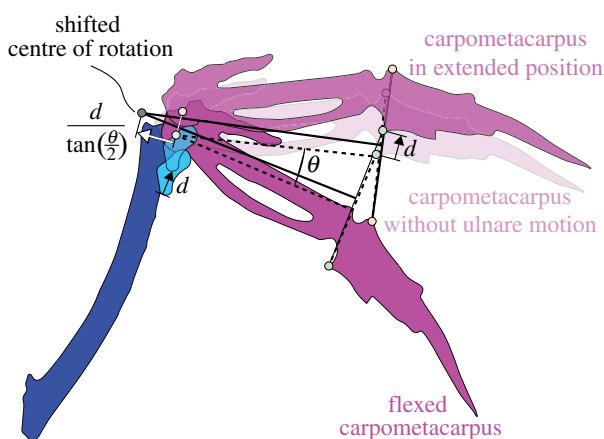
Figure 8. The shifted centre of rotation in a crossed four-bar simulates the effect of a slider joint, the ulnare, which enables it to fit the measured skeletal motion data better. We demonstrate this mathematically using the Reuleaux method, which is a geometric construction to find the centre of rotation in two dimensions [44]. By only rotating the carpometacarpus (light pink), the centre of rotation is approximately where expected—at the end of the ulna and inside the condyle of the carpometacarpus. If instead, the carpometacarpus both rotates and translates (dark pink), then the centre of rotation is shifted anterior of the condyle of the carpometacarpus by a distance of $d/\tan(\theta/2)$. This combination of rotation and translation corresponds to the effect of the sliding ulnare in the pigeon wing, which pushes the centre of rotation out.

and ulnare joints by fusing them with the radius and ulna respectively in their fully extended position. The tracking performance of this four-bar model (no wrist joints, 6 degrees of freedom) is significantly worse (table 1, figure 6); therefore, the wrist joints serve a measurable function. To test if both wrist joints contribute equally to the improved tracking performance, we released their degree of freedom individually in the four-bar model with the fused wrist (just radiale or just ulnare, figure 6). This test shows that including the ulnare joint significantly improves tracking performance of the measured skeletal motion for each pigeon, while the radiale only provides significant improvement in one pigeon. This makes sense because the rotation of the radiale around the end of the radius contributes only a second rotation, while the ulnare contributes sliding motion along the end of the ulna, which shifts the centre of rotation with the carpometacarpus (figure 4) and extends the wingspan.

While the simplified six-bar model with fused wrist joints indicates that wrist bones are necessary to accurately model wing morphing, it is possible to create better four-bar mechanisms by optimizing their joint locations and types directly. Remarkably, if we directly optimize a four-bar mechanism from the motion capture data, the resulting mechanism requires the radius and ulna to cross. This simulates the wrist function, but is anatomically unrealistic. The crossing mechanism connects the optimized joint locations with the
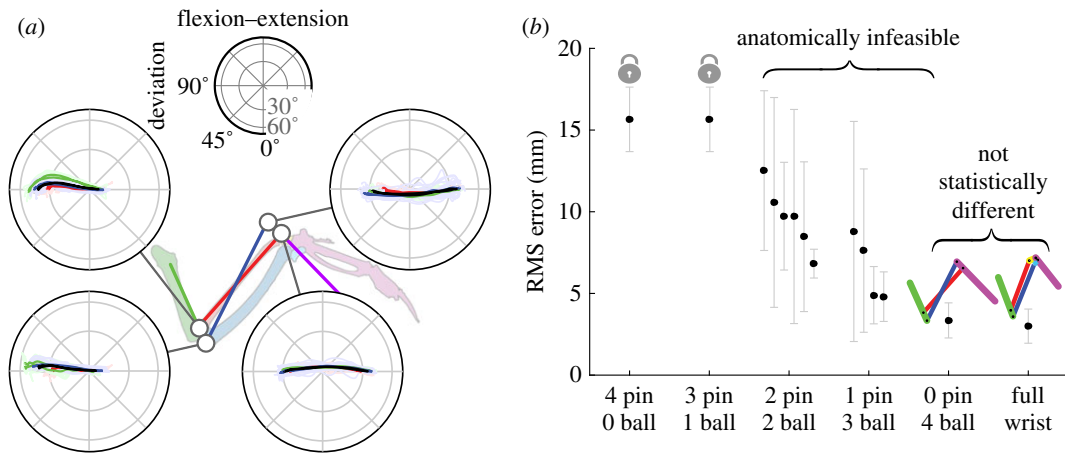
Figure 9. Flexion and extension of the avian wing skeleton is best modelled by a six-bar mechanism, because all corroborated four-bar mechanisms are locked or require the ulna and radius to cross for minimal RMS error—regardless of all possible permutations of spherical versus pin joints. (a) A crossed four-bar mechanism with four spherical joints best represents the measured skeletal motion based on least-squares error minimization. The anatomically unrealistic crossing of the ulna and radius places the centre of rotation of the ulna–carpometacarpus joint in front of the radius–carpometacarpus joint which simulates the effect of the sliding ulnare wrist bone. The associated spherical joint motion paths are more similar for all three pigeons than found for the anatomically realistic six-bar mechanism (figure 5). (b) Evaluation of all possible combinations of pin and spherical (ball) joints shows that four-bar mechanisms are either locked or require the radius and ulna to cross to accurately replicate the measured skeletal motion. In contrast, the least-squares error minimization algorithm requires the radius and ulna of the six-bar mechanism to be parallel, which is not only anatomically realistic, but also results in the lowest RMS error. Remarkably, the crossed four-bar mechanism with four spherical joints can achieve a similarly low RMS error as the six-bar mechanism with no statistical difference when pooled (pooled, $n = 3$; individually $p = 0.44$ for pigeon 1, $p = 0.03$ for pigeon 2, $p = 0.16$ for pigeon 3).

shortest possible links (figure 7b), aligning the ulna and radius along the links of this virtual mechanism when applying parsimony. An even simpler three-dimensional four-bar mechanism with four pin joints is unable to move along the bone motion paths (figure 7a,c). The pin joints lock the mechanism, because it has negative two degrees of freedom along the highly three-dimensional bone motion paths (figure 2). In contrast, a four-bar mechanism with four spherical joints (figure 7b) tracks the measured skeletal kinematics well (figure 7c). However, the least-squares error minimization finds that the joint centre connecting the ulna with the carpometacarpus needs to be positioned anterior to the radius–carpometacarpus joint, forcing the ulna and radius to crosses. Additionally, we determined that the optimized centre of rotation of the ulna no longer lies within the condyle of the carpometacarpus. These outcomes of the least-squares error minimization are thus anatomically unrealistic. To understand this, we further analysed this solution mathematically and found that the crossing links simulate the function of the sliding ulnare in the wrist. When the ulnare slides along the ulna, it causes the average centre of rotation between the ulna and carpometacarpus to shift anteriorly (figures 8 and 9a). The sliding motion of the ulnare is confirmed by the μCT scans (figure 4). Further, for all permutations of pin and spherical joint combinations we find that the optimized four-bar mechanism either locks or crosses (figure 9b). This shows how all hypothesized four-bar mechanisms in the literature lock in three dimensions (because they include only pin joints), result in anatomically unrealistic mechanisms that simulate the wrist (optimized spherical joints) or are imprecise (four-bar model based on anatomy with fused wrist joints) when recreating measured skeletal motion. Therefore, we conclude that the wrist bones are an integral part of the measured wing morphing mechanism, which requires a full-fledged six-bar mechanism to model avian wing motion and anatomy in concert (electronic supplementary material, table S4). It has not escaped our

attention, however, that the crossed four-bar mechanism is as accurate (figure 9b) and potentially simpler to embody in engineering morphing wing design and multiphysics simulations of avian flight (electronic supplementary material, table S5). However, the six-bar mechanism is a better choice if precise joint centres and moment arms between the bones are needed. Future studies could test how well the degrees of freedom in the joints of the six-bar mechanism capture wing pronation and supination, flapping motion, as well as fully folding the wing against the body.

4. Conclusion

Based on detailed wing morphology and motion measurements for three pigeons, we corroborated a three-dimensional six-bar mechanism that models the morphing function of the avian wing skeleton. The two additional bars, compared to the four-bar paradigm, are essential to model wrist function. The model is robust to all simplifying manipulations: inclusion of three-dimensional spherical joints to form the elbow at the humerus and the wrist at the carpometacarpus, as well as the additional two-dimensional degrees of freedom wrist joints with the radius and ulna, are essential to recreate the measured function. Both the six-bar manipulations and the four-bar optimizations point at the pivotal role of the sliding ulnare to interpret wrist function and recreate avian wing morphing motion. Therefore, the ubiquitous 'drawing parallels' explanation of avian forelimb function in textbooks on animal flight [5,19] and functional morphology [6], as well as natural history museum displays (e.g. the Smithsonian National Museum of Natural History, 2016) need to be revised. The new six-bar model with a functional wrist can help interpret fossils [29] and bird development [45]. It may also help inform more effective treatment plans for injured birds [22,23]. Finally, both the biologically realistic six-bar and the anatomically unrealistic

crossed four-bar model offer quantitative inspiration for engineering morphing wing design [30–33].

References

1. Bergmann C. 1839 Uber die Bewegungen von Radius und Ulna am Vogelflugel. Arch. Anat. Physiol. wiss Med. 6, 296–300.

2. Fisher HI. 1957 Bony mechanism of automatic flexion and extension in the pigeon's wing. Science 126, 446. (doi:10.1126/science.126.3271.446)

3. Coues E. 1871 Mechanism of flexion and extension in birds' wings. Am. Nat. 5, 513–514. (doi:10.1086/270813)

4. Nachtigall W. 1985 Warum die Vögel fliegen. Rasch und Rohring.

5. Norberg UMU. 1990 Vertebrate flight, ch. 11, pp. 180–236. Berlin, Germany: Springer-Verlag. (doi:10.1007/978-3-642-83848-4_11)

6. Liem K, Walker W, Grande W, Liem L. 2001 Functional anatomy of the vertebrates: an evolutionary perspective, 3rd edn. Fort Worth, TX: Cengage Learning.

7. Parslew B, Crowther WJ. 2010 Simulating avian wingbeat kinematics. J. Biomech. 43, 3191–3198. (doi:10.1016/j.jbiomech.2010.07.024)

8. Hedrick TL, Tobalske BW, Ros IG, Warrick DR, Biewener AA. 2012 Morphological and kinematic basis of the hummingbird flight stroke: scaling of flight muscle transmission ratio. Proc. R. Soc. B 279, 1986–1992. (doi:10.1098/rspb.2011.2238)

9. Parslew B. 2015 Predicting power-optimal kinematics of avian wings. J. R. Soc. Interface 12, 20140953. (doi:10.1098/rsif.2014.0953)

10. Baier DB, Gatesy SM, Dial KP. 2013 Three-dimensional, high-resolution skeletal kinematics of the avian wing and shoulder during ascending flapping flight and uphill flap-running. PLoS ONE 8, e63982. (doi:10.1371/journal.pone.0063982)

11. Tobalske BW, Warrick DR, Clark CJ, Powers DR, Hedrick TL, Hyder GA, Biewener AA. 2007 Three-dimensional kinematics of hummingbird flight. J. Exp. Biol. 210, 2368–2382. (doi:10.1242/jeb.005686)

12. Vazquez RJ. 1994 The automating skeletal and muscular mechanisms of the avian wing (Aves). Zoomorphology 114, 59–71. (doi:10.1007/BF00574915)

13. Vazquez RJ. 1992 Functional osteology of the avian wrist and the evolution of flapping flight. J. Morphol. 211, 259–268. (doi:10.1002/jmor.1052110303)

14. Pennycuick C. 1968 A wind-tunnel study of gliding flight in the pigeon Columba livia. J. Exp. Biol. 49, 509–526.

15. Lentink D et al. 2007 How swifts control their glide performance with morphing wings. Nature 446, 1082–1085. (doi:10.1038/nature05733)

16. Tucker VA. 1987 Gliding birds: the effect of variable wing span. J. Exp. Biol. 133, 33–58.

17. Warrick DR, Bundle MW, Dial KP. 2002 Bird maneuvering flight: blurred bodies, clear heads. Integr. Comp. Biol. 42, 141–148. (doi:10.1093/icb/42.1.141)

18. Tobalske BW. 2007 Biomechanics of bird flight. J. Exp. Biol. 210, 3135–3146. (doi:10.1242/jeb.000273)

19. Pennycuick CJ. 2008 Modelling the flying bird. Theoretical Ecology Series. Burlington, MA: Academic Press.

20. Pennycuick CJ. 2008 Theory as the basis for observation. In Modeling the flying bird (ed. A Hastings), pp. 409–441. Burlington, MA: Elsevier.

21. Chatterjee S. 2015 The rise of birds, 2nd edn. Baltimore, MD: Johns Hopkins University Press.

22. Beaufrère H, Ammersbach M, Nevarez J, Heggem B, Tully Jr TN. 2012 Successful treatment of a radioulnar synostosis in a Mississippi kite (Ictinia mississippiensis). J. Avian Med. Surg. 26, 94–100. (doi:10.1647/2011-008.1)

23. Rupiper DJ, Ramsay E. 1993 Radial ostectomy in a barn owl. J. Assoc. Avian Vet. 7, 160. (doi:10.2307/30135053)

24. Baier DB, Gatesy SM, Jenkins FA. 2007 A critical ligamentous mechanism in the evolution of avian flight. Nature 445, 307–310. (doi:10.1038/nature05435)

25. Gonzalez RV, Buchanan TS, Delp SL. 1997 How muscle architecture and moment arms affect wrist flexion-extension moments. J. Biomech. 30, 705–712. (doi:10.1016/S0021-9290(97)00015-8)

26. Holzbaur KRS, Murray WM, Delp SL. 2005 A model of the upper extremity for simulating musculoskeletal surgery and analyzing neuromuscular control. Ann. Biomed. Eng. 33, 829–840. (doi:10.1007/s10439-005-3320-7)

27. Gustus A, Stillfried G, Visser J, Jörntell H, van der Smagt P. 2012 Human hand modelling: kinematics, dynamics, applications. Biol. Cybern. 106, 741–755. (doi:10.1007/s00422-012-0532-4)

28. Metcalf CD, Notley SV, Chappell PH, Burridge JH, Yule VT. 2008 Validation and application of a computational model for wrist and hand movements using surface markers. IEEE Trans. Biomed. Eng. 55, 1199–1210. (doi:10.1109/TBME.2007.908087)

29. Sullivan C, Hone DWE, Xu X, Zhang F. 2010 The asymmetry of the carpal joint and the evolution of wing folding in maniraptoran theropod dinosaurs. Proc. R. Soc. B 277, 2027–2033. (doi:10.1098/rspb.2009.2281)

30. Wissa A, Grauer J, Guerreiro N, Hubbard J, Altenbuchner C, Tummala Y, Frecker M, Roberts R. 2015 Free flight testing and performance evaluation of a passively morphing ornithopter. Int. J. Micro Air Veh. 7, 21–40. (doi:10.1260/1756-8293.7.1.21)

31. Grant DT, Abdulrahim M, Lind R. 2006 Flight dynamics of a morphing aircraft utilizing independent multiple-joint wing sweep (IJMAV). Int. J. Micro Air Veh. 2, 91–106. (doi:10.1260/1756-8293.2.2.91)

32. Hara N, Tanaka K, Ohtake H, Wang HO. 2009 Development of a flying robot with a pantograph-based variable wing mechanism. IEEE Trans Robot. 25, 79–87. (doi:10.1109/TRO.2008.2008736)

33. Stowers AK, Lentink D. 2015 Folding in and out: passive morphing in flapping wings. Bioinspir. Biomim. 10, 25001. (doi:10.1088/1748-3190/10/2/025001)

34. Konow N, Cheney JA, Roberts TJ, Waldman JRS, Swartz SM. 2015 Spring or string: does tendon elastic action influence wing muscle mechanics in bat flight? Proc. R. Soc. B 282, 20151832. (doi:10.1098/rspb.2015.1832)

35. Brainerd EL, Baier DB, Gatesy SM, Hedrick TL, Metzger KA, Gilbert SL, Crisco JJ. 2010 X-ray reconstruction of moving morphology (XROMM): precision, accuracy and applications in comparative biomechanics research. J. Exp. Zool. A Ecol. Genet. Physiol. 313, 262–279.

36. Hammersley JM, Handscomb DC. 1965 Monte Carlo methods. Methuen's Monogr. 18, 55.

37. Pennycuick CJ. 2015 The flight of birds and other animals. Aerospace 2, 505–523. (doi:10.3390/aerospace2030505)

38. Gamage SSHU, Lasenby J. 2002 New least squares solutions for estimating the average centre of rotation and the axis of rotation. J. Biomech. 35, 87–93. (doi:10.1016/S0021-9290(01)00160-9)

39. Marghitu DB. 2005 *Kinematic chains and machine components design*. Burlington, MA: Elsevier Academic Press.

40. MacWilliams BA. 2008 A comparison of four functional methods to determine centers and axes of rotations. *Gait Posture* **28**, 673–679. (doi:10.1016/j.gaitpost.2008.05.010)

41. Delp SL, Anderson FC, Arnold AS, Loan P, Habib A, John CT, Guendelman E, Thelen DG. 2007 OpenSim: open source to create and analyze dynamic simulations of movement. *IEEE Trans. Biomed. Eng.* **54**, 1940–1950. (doi:10.1109/TBME.2007.901024)

42. Li ZM, Kuxhaus L, Fisk JA., Christophel TH. 2005 Coupling between wrist flexion-extension and radial-ulnar deviation. *Clin. Biomech.* **20**, 177–183. (doi:10.1016/j.clinbiomech.2004.10.002)

43. Gamage SSHU, Lasenby J. 2002 New least squares solutions for estimating the average centre of rotation and the axis of rotation. *J. Biomech.* **35**, 87–93. (doi:10.1016/S0021-9290(01)00160-9)

44. Reuleaux F. 1875 Theoretische Kinematik: Grundzuge einer Theorie des Maschinenwesens. Vol 1. Vieweg und Sohn.

45. Botelho JF, Ossa-Fuentes L, Soto-Acuña S, Smith-Paredes D, Nuñez-León D, Salinas-Saavedra M, Ruiz-Flores M, Vargas AO. 2014 New developmental evidence clarifies the evolution of wrist bones in the dinosaur–bird transition. *PLoS Biol.* **12**, e1001957. (doi:10.1371/journal.pbio.1001957)